Calibrated Thermal Microscopy of the Tool–Chip Interface in Machining

M. A. Davies , H. Yoon , T. L. Schmitz , T. J. Burns & M. D. Kennedy

Published online: 07 Feb 2007.

Submit your article to this journal ⬈

Article views: 152

View related articles ⬈

Citing articles: 33 View citing articles ⬈

Calibrated Thermal Microscopy of the Tool–Chip Interface in Machining

M. A. Davies,[1],* H. Yoon,[2] T. L. Schmitz,[2] T. J. Burns,[2] and M. D. Kennedy[2]

[1]Center for Precision Metrology, University of North Carolina at Charlotte, Charlotte, North Carolina, USA
[2]National Institute of Standards and Technology, Gaithersburg, Maryland, USA

ABSTRACT

This paper presents the results of calibrated, microscopic measurement of the temperature fields at the tool–chip interface during the steady-state, orthogonal machining of AISI 1045 steel. The measurement system consists of an infrared imaging microscope with a 0.5 mm square target area, and a spatial resolution of less than 5 μm. The system is based on an InSb 128 × 128 focal plane array with an all-reflective microscope objective. The microscope is calibrated using a standard blackbody source from NIST. The emissivity of the machined material is determined from the infrared reflectivity measurements. Thermal images of steady state machining are measured on a diamond-turning class lathe for a range of machining parameters. The measurements are analyzed by two methods: 1) energy flux calculations made directly from the thermal images using a control–volume approach; and 2) a simplified finite-difference simulation. The standard uncertainty of the temperature measurements is ± 52°C at 800°C.

*Correspondence: M. A. Davies, Center for Precision Metrology, University of North Carolina at Charlotte, Charlotte, NC 28223-0001, USA; Fax: (704) 687-3246; E-mail: madavies@uncc.edu.

www.dekker.com

INTRODUCTION

Machining operations comprise a substantial portion of the world's manufacturing infrastructure. For example, Merchant (1998) estimated that ''in industrialized nations, the cost of machining amounts to more than 15 percent of the total value of all products produced by their entire manufacturing industry.'' However, despite its obvious economic and technical importance, the ability to make general, a priori predictions about the outcome of machining processes remains poor (van Luttervelt et al., 1998). Thus, extensive empirical testing is needed to develop new machining processes, and this need has been cited by private sector representatives as a major factor in the cost of developing new production processes (Furness, 1998).

The lack of understanding of machining operations stems from the relative complexity of the material removal mechanism. It is well established that the material flow occurring during chip formation is characterized by high rates of strain (approaching $10^6 s^{-1}$), large thermal gradients ($1000°C/\mu m$) and high stresses (10 MPa). Such extreme conditions of plasticity are rarely encountered, except in conditions of ballistic impact (Meyers). Detailed simulation of the stress, strain, strain-rate and temperature distributions under these conditions requires both complex data on material behavior (Childs, 1997) and advanced numerical and analytical methods. Because of the difficulties involved in modeling the machining process at this fundamental level, semi-empirical mechanics-based (lumped-parameter) models of machining have been developed. These models rely upon empirical databases of cutting force coefficients in orthogonal machining operations to predict the results of more complex cutting geometry (Altintas, 2000; Amarego and Brown, 1969). They have great practical utility for predicting the forces and dynamics of machining, but they do not predict distributions of important quantities such as temperature. Furthermore, the input databases are extensive and must be regenerated as tool and workpeice materials change.

Other more fundamental modeling methods seek to make analytical predictions of machining operations with a smaller set of input data that are more closely connected with the basic physical properties of the material. The most successful of these analytical models are based on slip-line field theories (Oxley, 1989). While these methods are capable of predicting some aspect of the stress distributions in machining and can account for temperature changes, they are limited to continuous chip formation.

More recently, finite-element methods have emerged as a potentially powerful tool for simulating machining processes (Ceretti et al., 1996; Marusich and Ortiz, 1995; Movahhedy et al., 2000; Strenkowski and Carroll, 1986). These models produce detailed predictions of the distributions of temperature, stress, and strain. However, the time for each simulation is long and requires considerable computational capability. Furthermore, the accuracy of these simulations relies on materials data that is expensive and difficult to generate and often not valid for the range of conditions encountered in machining. Furthermore, a quantitative assessment of the accuracy of these models is severely limited by a lack of temporally and spatially resolved experimental data. This paper describes the results of a research effort with the goal of filling some of this void in experimental data by generating accurate, high-resolution, high-bandwidth microscopic temperature measurements of the tool–chip interface using infrared micro-scopy. Such data will not only be useful in evaluating the predictive performance of

current machining models, but may also be of importance in the determination of fundamental materials data from simple machining tests.

Temperature measurement has been a major focus of machining research for several decades. Use of the tool–chip interface as a thermocouple was one of the first methods aimed for estimating machining temperature. This method was first explored by Herbert (1926), Boston and Gilbert (1935) and Trigger (1948). Recent work with comprehensive references include Stephenson (1993) and Ivester et al. (2000) who used the technique in an effort to assess the predictive capability of machining models. This method has the important advantages of being relatively easy to implement and being applicable to complex, non-orthogonal cutting geometry. However, the results are difficult to interpret, the associated uncertainties are large, and the method does not generate a temperature distribution. Spatially resolved measurements of temperature distributions that are required for quantitative assessment of the predictive capability of current models are much more difficult to obtain. Trent (1991) was able to estimate temperature distributions in high-speed steel tools through micro-hardness measurements that could be correlated to thermally driven changes in the microstructure of the tool. These measurements were limited to the determination of time-averaged temperature distributions in the tool and were of limited spatial resolution due to the size of the hardness indenter. Using infrared sensitive film and a microscope, Boothroyd (1961, 1963) was able to estimate temperature distributions in the tool and chip. Compared with modern miniature electronic sensors, this method was limited in spatial and temporal resolution; the spatial resolution of these measurements was approximately 50 micrometers. More recent measurements have utilized solid-state electronic devices sensitive to infrared radiation to make non-contact temperature measurements with very high bandwidth exceeding five megahertz. These techniques have also been used to measure temperatures during high-strain-rate transient deformations in Kolsky bar tests (Hartley et al., 1987) with 20 micrometer resolution and bandwidth of nearly ten megahertz. These methods show great promise for high spatial and temporal resolution measurements of machining temperatures. However, making such measurements with spatial resolutions better than ten micrometers requires very well-controlled machining conditions.

The reasons for revisiting infrared temperature measurements of machining are numerous and compelling. First, the temporal and spatial resolution of current numerical models far exceeds the resolutions attained in published experimental temperature data. Second, despite past efforts, the data on temperature distributions in machining is relatively sparse and incomplete (Jawahir, 1999). Third, improvements in non-contact thermometry equipment and precision machine-tools make more accurate high-bandwidth and high-resolution measurements possible. Finally, there is a need for a more thorough assessment of the *uncertainties* in experimental measurements of temperature in machining without which *quantitative comparisons* between measurements and numerical models are not meaningful.

This paper describes the development of a thermal microscopy system based upon a commercially available, liquid nitrogen cooled Indium Antimonide (InSb) focal plane array. This system is utilized to measure temperatures in orthogonal cutting of AISI 1045 steel on a precision lathe with an air-bearing spindle. This process was chosen for three main reasons: 1) it is the focus of many recent modeling efforts; 2) AISI 1045 steel is easily attainable and is similar to the C45 steel used in the ISO 3685 Tool Life

Testing Standard; 3) relatively complete material response models of AISI 1045 are available in the open literature; and 4) AISI 1045 steel is also the focus of the recent industry-led *Assessment of Machining Models* benchmarking activity. The temperature measurement system and the machining experiments are described in Materials and Experimental Methods. In Results, the calibration procedure, measurements of workpiece emissivity and the system uncertainties are described. In Analysis and Discussion, measurements of orthogonal cutting for a range of parameter values are presented. These results are analyzed in Conclusion using two approaches: 1) an energy calculation method based on a control volume approach; and 2) a comparison to a simplified numerical method with plausible parameters. Based upon the evaluation of uncertainties, the results are believed to be accurate to better than ± 52°C over the entire temperature range 20°C to 800°C with proportionately smaller uncertainties at lower temperatures.

MATERIALS AND EXPERIMENTAL METHODS

The experimental apparatus consisted of two components, the micro-pyrometry system and the machining system. Successful measurements required an accurate calibration of the micropyrometry system, measurement of the workpiece emissivity, and an accurate and rigid orthogonal cutting system. Each of the major experimental components is detailed in this section.

Machining Platform

Cutting experiments were conducted on a two-axis diamond turning machine that was modified to incorporate the thermal microscopy system as shown in Figure 1. A simplified orthogonal cutting (approximately plane strain) operation was generated by advancing a tool toward the end of a 1.5 mm thick tube. This generated a chip of rectangular cross-section with a thickness of f/Ω, where Ω denotes the rotation rate of the spindle in revolutions per second and f denotes the axis feed rate in micrometers per second. The cutting edge of the tool had a width approximately three times greater than that of the tube and had fixed rake and clearance angles of 0 and 5 degrees, respectively. The diamond turning machine used in the experiments was capable of high-accuracy, unidirectional, single-axis motions with a positioning accuracy better than 20 nanometers. The spindle error motions were less than 10 nanometers. These accuracies are much better than those associated with conventional machine tools and were important to ensure that the workpiece would remain in focus during the thermal measurements. The major limitation of this system is the relatively low spindle power of approximately 1.25 kW which restricted the attainable range of cutting conditions.

The workpiece was an AISI 1045 steel tube. The chemical composition of the material was independently verified to be: 0.45 percent Carbon, 0.70 percent Manganese, 0.26 percent Silicon, 0.008 percent Sulfur, 0.009 percent Phosphorus with the balance being Iron. To minimize variations in material properties that can result from drawing processes, the tube was machined from a solid bar of steel. Focus and emissivity variations associated with workpiece eccentricity and roughness were minimized in two steps: 1) the outer surface of the tube was re-machined on the diamond turning
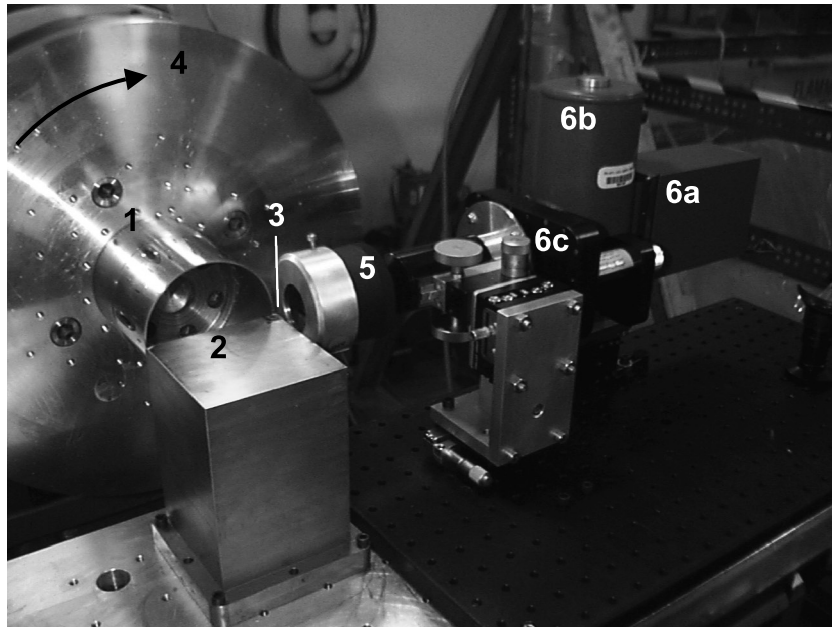
Figure 1. Experimental system for measuring machining temperatures in orthogonal cutting including: (1) polished AISI 1045 steel tube; (2) monolithic steel tool post; (3) tungsten carbide cutting tool insert; (4) diamond-turning class air-bearing spindle; (5) 15 × reflecting objective; (6) thermal imaging camera consisting of focal plane array (a), nitrogen container (b) and wavelength notch filter (c).

machine; 2) the surface of the tube was then polished on the machine using a sequence of fine-grained Silicon Carbide papers followed by lapping with cubic-Boron Nitride (CBN) slurries with average grit size ranging from 6 μm to 0.75 μm. The final surface finish was estimated to have a root-mean-square surface roughness of 40 nm. Using this procedure, positional variation of the surface of the tube during operation of the spindle was limited to much less than 1 μm. The final length, diameter and thickness of the tube were 101.5 mm, 101.5 mm and 1.5 mm, respectively. A cemented, tungsten carbide tool was mounted to a monolithic steel tool-post designed to maximize system stiffness. The tool was custom ground so that the desired image plane of the tool was perpendicular to the optical axis of the microscopy system.

Measurement System

The thermal imaging micro-pyrometer (MIPY), shown in Figure 1, was constructed using a commercial 128 by 128 InSb focal plane array (FPA) from Santa Barbara Focal Plane[a] with an all-reflective 0.5 NA, microscope objective with a magnification of 15 times which directly focused the image of the object on the FPA. The objective was

---

[a]Use of commercial names does not imply endorsement by NIST.

mounted on a commercial microscope body and the FPA was attached to the rear output of the microscope. The front end of the objective, which was located approximately 25 mm from the cutting zone, was protected against contamination and damage using a sapphire window. The system was focused in two steps, first by visual alignments with the FPA replaced by an eyepiece, and then by replacing the FPA, backlighting with a heat source and adjusting the focus for image sharpness. The InSb detector was used with a broad-band spectral filter, which transmits from 3 μm to 5 μm in wavelength. The individual pixels in the FPA were deposited 50 μm apart. Based upon the magnification, the theoretical spatial resolution of the system was found to be approximately 3.3 μm. In reality, the resolution is limited to the wavelength of the detected light from the Rayleigh criterion. The actual spatial resolution was further verified to be slightly better than 5 μm using a chrome-on-glass USAF 1951 resolution target that was illuminated from behind using a heat source. Under the calibration and operating conditions, the field-of-view of the system was estimated to be approximately 480 μm square.

System Calibration

The material temperatures from the optically measured or the radiance temperatures were found using the following procedure. The radiance temperature responsivity of the MIPY was determined using a blackbody with known contact temperatures and emissivity. In this method, a small blackbody with an emissivity of 0.99 and an aperture of 2 mm in diameter was placed at the focus of the MIPY. The temperature of the blackbody was measured using a type-S thermocouple with the reference junction immersed in an ice water bath. This temperature was varied at step intervals from about 100°C to 700°C. The thermal images of the blackbody and the ambient room-temperature background were measured at each temperature step. Since both the frame rate and the integration time can be separately changed to avoid saturation of the FPA pixel elements, measurements were performed at a set frame rate by varying the integration time as the blackbody temperature was changed. All the measurements were converted to net count rates R_b (related to photon counts per second) by subtracting the room-temperature background and dividing by the integration time. The net count rates as a function of temperature were fitted using an interpolating function. The interpolating function was the Sakuma equation (Sakuma and Kobayashi, 1996),

$$R_b = P_1 e^{\frac{-C_2}{P_2 T + P_3}} \tag{1}$$

where T is the temperature in Kelvin (K), C_2 is the second radiation constant and P_1, P_2 and P_3 are fitting parameters given by $P_1 = 3179000$ counts/s, $P_2 = 4133$ and $P_3 = 0.2503$. The fit of Eq. 1 to the experimental values resulted in negligible residuals at all the separate temperature calibrations. Repeat calibrations separated by a few weeks and then again separated by a few months showed that the reproducibility of the radiance temperature measurements of the blackbody using the MIPY was better than ± 0.5 percent. The uncertainty of the thermocouple is also included in this calibration uncertainty estimate. A typical set of calibration data and the associated calibration curve generated by the Sakuma equation is shown in Figure 2.
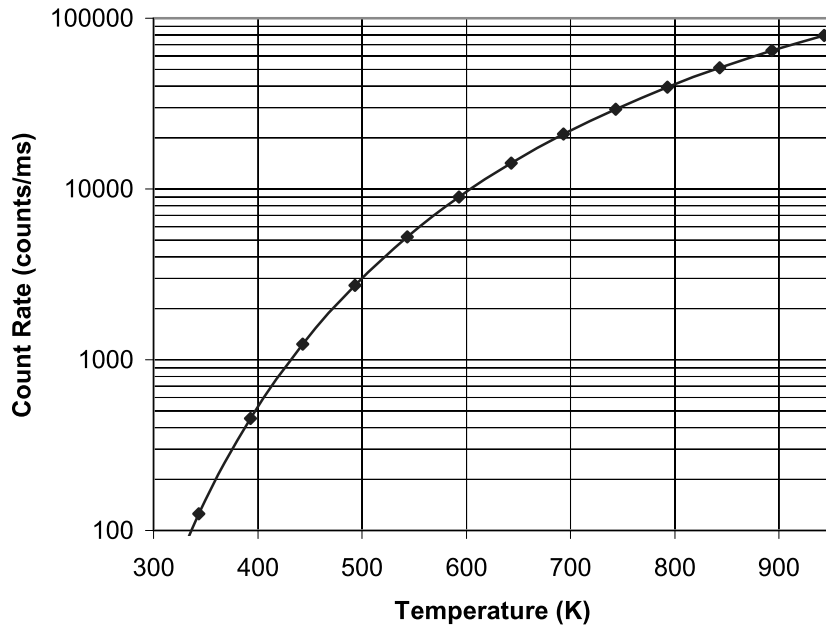
Figure 2. Calibration curve and fit using the Sakuma equation.

Emissivity

Since the emissivity of the material is an unknown function of the temperature, separate measurements of the spectral reflectance were used to determine the emissivity. The reflectance of a polished steel sample, shown in Figure 3(a), was measured in the NIST IR spectral reflectivity facility using an FT-IR spectrometer, and the spectral emissivity at room temperature was set to be equal to $1 - \rho$, where ρ is the 8°/h reflectance.[b] From the reflectance measurements, the band average emissivity between 3 μm to 5 μm was determined to be 0.14. Since the emissivity of most metals including steel increases with increasing temperature, a relationship between emissivity and raw signals was determined from published values shown in Figure 3(b) to assign a higher emissivity to the regions with higher radiance temperatures. The emissivity as a function of temperature was fit using a parabolic curve of the following form,

$$\varepsilon = K_3 + K_2 T + K_1 (T - K_4)^2 \tag{2}$$

where $K_1 = -7.829\text{e} - 08 \ \text{K}^{-2}$, $K_2 = 2.2926\text{e} - 004 \ \text{K}^{-1}$, $K_3 = 0.075301$ and $K_4 = 0.0023049$ K.

---

[b]In the 8°/h measurement, light is incident on the sample along a line that is 8 degrees from the surface normal and the reflected light is measured over an entire surrounding hemisphere.
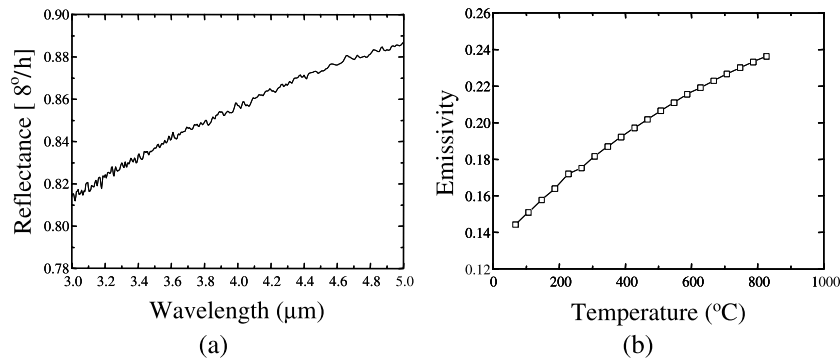
Figure 3. (a) Reflectance versus wavelength and (b) emissivity versus temperature for AISI 1045 steel.

While the emissivity of the tool material is expected to be substantially greater than that of the workpiece material (approximately 0.4), it was found that after a few experiments, the local region of the tool in the field of view became coated with a thin, reflective layer of workpiece material. This phenomenon had the unforseen advantage that the tool and workpiece had essentially the same emissivity.

Due to changes from the initital polished state during the experiment, the emissivity of the material is a major source of uncertainty in the experiments. Two effects are of particular concern: 1) changes in the surface due to plastic deformation; and 2) oxidation. The first effect has been studied in Kolsky bar experiments that have examined the dynamic formation of shear bands in steel using methods similar to those employed here (Jawahir, 1999). These experiments have reported that the difference in emissivity between polished and plastically deformed AISI 1018 steel decreased as a function of temperature, and was less than ten percent at temperatures above 200°C. These experiments also found little oxidation driven variations in emissivity occuring during the deformation possibly due to the low thickness of the oxide layers relative to the wavelength of the light being measured. Although these results are promising, the potential uncertainty in sample emissivity remains dominant in our estimates of overall uncertainty as discussed below.

Iterative Approach to Temperature Determination

Because the emissivity is related nonlinearly to the thermodynamic temperature, and the thermodynamic temperature is nonlinearly related to the signal output of the detectors, the determination of thermodynamic temperature of the sample requires the solution of a transcendental equation of the following form.

$$R_m = \varepsilon(T)R_b(T) = \left(K_1(T - K_4)^2 + K_2T + K_3\right)\left(P_1 e^{-C_2/(P_2T+P_3)}\right) \tag{4}$$

This equation states that the measured signal is equal to the signal that would be obtained if the measured surface were a blackbody multiplied by the surface emissivity.

This equation is solved using an iterative technique with the following steps: 1) begin with an initial guess for the emissivity ε_0 equal to the mean emissivity from Figure 3(b), approximately 0.18; 2) calculate the equivalent blackbody signal by taking the output of each pixel and dividing by the assumed emissivity, ε_0; 3) estimate the thermodynamic temperature from the blackbody calibration curve; 4) using the estimated thermodynamic temperature, calculate a new estimate for the emissivity (denoted ε_i for iteration number i) from the emissivity versus temperature curve; 5) repeat the procedure until the difference between the previous estimated emissivity and the new estimated emissivity ($\varepsilon_i - \varepsilon_{I-1}$) is within a pre-specified error. In example test cases, this method was found to converge in five iterations to the correct temperature within one part in ten thousand. This was the tolerance used in calculating the temperatures reported below.

Uncertainty Analysis

The uncertainty in the temperature measurements presented in the next section has a number of components. These are summarized in Table 1. Since the errors will be largest at the higher temperatures, we chose to treat them at the maximum temperatures reported in the experimental results—approximately 800°C. Errors due to calibration of the system are the least significant. The magnitude of this error was determined from repeat calibrations that showed a standard deviation of approximately 0.5 percent over a period of 6 months. Thus, the error due to calibration at 800°C is approximately ± 4°C.

Table 1. Sources of uncertainty and combined standard uncertainty.

Source of uncertainty	Analysis type	Numerical estimate
Calibration of Thermal Imaging System	B	±4°C (±0.5 percent)
• Emissivity of Black Body		
• Curve Fitting		
• Stray Light		
Experimental Fluctuations	B	±15°C (±2 percent)
• Unmeasured changes in cutting conditions such as cutting speed, chip thickness and chip width.		
• Fluctuations in emissivity around the mean due to changes in local surface finish etc.		
• Stray light from chips and other sources		
• Changes in surface location causing variations in focus		
• Iterative Temperature Calculation		
Mean Emissivity Shift	A	±50°C (±6.1 percent)
• Surface Roughening		
• Surface Oxidation		
• Method of Measuring Emissivity (8°h versus f/1 measurements)		
COMBINED STANDARD UNCERTAINTY		±52°C

A more significant source of error is the fluctuations that occur due to the high-frequency changes in the surface that occur during the machining experiments. These may be movements of the surface that cause focus variations, rapid fluctuations in local surface roughness, stray light from the chip and/or environment, numerical errors in the iterative calculation of temperature described above, focal plane array nonuniformity and other effects. The effect of these on the determination of the mean temperature at each pixel can be determined directly from fluctuations in the experimental measurements. To quantify these errors, multiple experimental measurements of the same steady-state experimental conditions were made, measured signal was transformed to temperature using the iterative approach described above, and then the experimental uncertainty in the mean of these measurements at each pixel is calculated as described in the next section. Note that because the statistical analysis of the measurements is done after the transformation to temperature, this component of uncertainty also contains the small affect of numerical errors arising from the iterative determination of temperature from measured signal in the presence of temperature varying emissivity. As described in the next section, the contribution of this error is found to be approximately ± 15°C at 800°C or approximately ±2 percent.

The most significant error source is the uncertainty in the mean emissivity. The uncertainty in the emissivity has two major sources: 1) changes in the sample surface due to plastic deformation and oxidation; and 2) variations in emissivity with the angle of observation (i.e. emissivity is not lambertian as in the blackbody radiation). Oxidation is not expected to be a large contributor to uncertainty in emissivity because both the time over which the measurement is made and the residence time of the material in the field of view are on the order of 100 microseconds. Even at elevated temperatures (∼1000°C), the formation of a compact oxide layer on steel surfaces takes many seconds to develop (Palik, 1991). Furthermore, an extremely thick oxide layer of a thickness on the order of the wavelength of the light (3 μm to 5 μm) would be required to change the emissivity (for our measurements) significantly. This is unlikely.

The uncertainty in the mean emissivity due to plastic deformation was discussed above. Referring to other published results (Jawahir, 1999), an uncertainty of approximately ±10 percent of the measured emissivity value is assigned. According to Hartley et al. (1987), this represents a conservative estimate for the uncertainty that should decrease as temperature is increased. The second source of error is that the reflectance measurements were done in a 8°/h geometry, while in the experiments, the radiation is collected in f/1 or 45° geometry with a central obscuration due to the reflective objective. Metals have increasing emissivity at angles away from the normal. Thus the 8°/h reflectivity measurements will underestimate the mean surface reflectivity (overestimate the emissivity) seen over the 45 degree collection cone. For a polished 1045 steel sample, the measured normal reflectivity can be compared to those found using the angle-dependent Fresnel equations along with the published values for n and k of polished iron (Saeki et al., 1996). The measured emissivities and the calculated normal emissivities using the Fresnel equations are compared in Table 2 and show agreement to better than ±5 percent over all wavelengths. Combining these sources in quadrature, we estimate an overall uncertainty in average emissivity of between 10 percent and 15 percent.

To complete the uncertainty analysis, we must calculate the effect of the emissivity variation on the variation in the observed temperature using the expressions described

Table 2. The calculated normal emissivity values found using the published n and k values for polished iron and the angle-dependent Fresnel equations.

Wavelength (μm)	n	k	Calculated emissivity	Measured emissivity
3.0	4.39	10.1	0.1764	0.185
4.0	4.54	12.6	0.1430	0.145
5.0	4.59	15.4	0.1177	0.115

above. Since we don't have an explicit relationship for temperature as a function of the measured signal rate, calculation of the uncertainty in temperature as a result of emissivity variations cannot be done in the standard way. The details of this calculation are given in Appendix A. According to that analysis, a ±15 percent uncertainty in emissivity leads to about ±50 degree C uncertainty at a temperature of 800 degrees C.

Combining all of the uncertainty components in quadrature, we obtain an overall uncertainty of ±52 degrees C a temperature of 800 degrees C. This applies to all of the results given in the next section. Note that the errors (in degrees C) are smaller for lower temperatures.

RESULTS

The machining parameters shown in Table 3 were chosen to produce a continuous steady-state chip while not exceeding the power limitations of the spindle. In Table 3, *f* is the feed rate, *t* is the uncut chip thickness (depth of cut), t_c is the cut chip thickness, *w* is the chip width, and *V* is the cutting (surface) speed. The uncertainty on these parameters is ± 5 μm/s, ±10 μm, ±50 μm, and ±0.05 m/s respectively.

Figure 4 shows the results of a measurement made under the first set of conditions in Table 3. This set of measurements was used to quantify the uncertainty due to experimental fluctuations occurring during the experiments. The image was generated from fifty frames measured at approximately 0.25 second intervals during a single experiment. Nine of these fifty frames were corrupt due to the passage of a burr through the cutting region. The remaining 41 frames were first converted to temperature using the

Table 3. Machining parameters and measured cut chip thickesses. Parameters were chosen to produce a range of continuous chip formation within the power limitations of the machine. Uncertainties on the cutting parameters are as follows: ±5 micrometers on *f*, ±2 micrometers on *t*, ±10 micrometers on t_c.

Experiment number	f (μm)	t (μm)	t_c (μm)	w (μm)	V (m/s)
1	341	37	125	1600	3.2
2	554	48	160	1500	3.7
3	462	40	145	1500	3.7
4	358	31	125	1500	3.7
5	266	23	100	1500	3.7
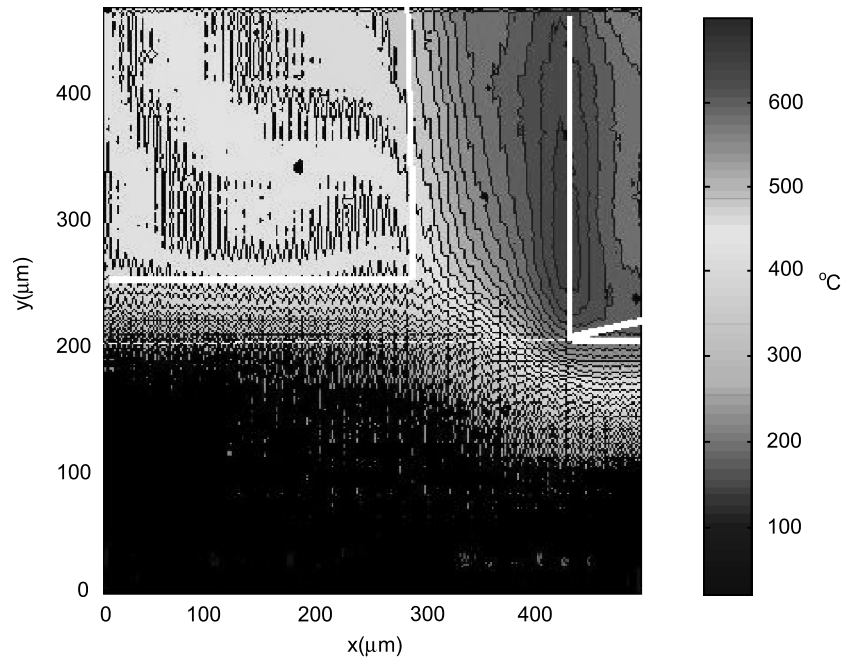
Figure 4. Mean of 41 thermal measurements of steady-state machining under experiments 1 in Table 2. The maximum standard error due to experimental fluctuations was less than ± 14 C for the region around the tool chip interface.

iterative scheme described above. Figure 4 shows the mean of these 41 temperature measurements. Since the tool remains fixed in the image, it was possible to superimpose an outline based upon thermally back lit images while no cutting was occurring. The chip and workpiece outline have also been superimposed using the uncut chip thickness and the measured cut chip thickness. The high temperatures shown in the region bounded by the workpiece and chip free surfaces are the result of imaging of the ''free'' surface of the chip. Such an effect could result from: 1) bulging of the back side of the chip during machining; 2) slight misalignment between the tool cutting edge and the optical axis of the microscope; and 3) stray and reflected light. This hypothesis is consistent with the apparent ''kinks'' in the isotherms, which indicate a transition from the side image of the chip to the back surface image.

The measurement shows many of the qualitative aspects of steady-state chip formation that have been previously measured using coarser resolution (Boothroyd, 1961, 1963; Trent, 1991). The peak temperature of about 675 degrees C develops along the rake face at a point about 140 micrometers from the leading edge. Because heat transfer is dominated by conduction in the tool and a mass transfer in the chip, the magnitude of the thermal gradients is much greater in the chip than in the tool. Furthermore, the workpiece surface left behind after machining also has a high temperature of nearly 500 degrees C, and still has not cooled completely when it enters the cutting region again at temperatures up to 350 degrees C. This observation is critical to correct completion of the energy calculations detailed below.

(a)

(b)
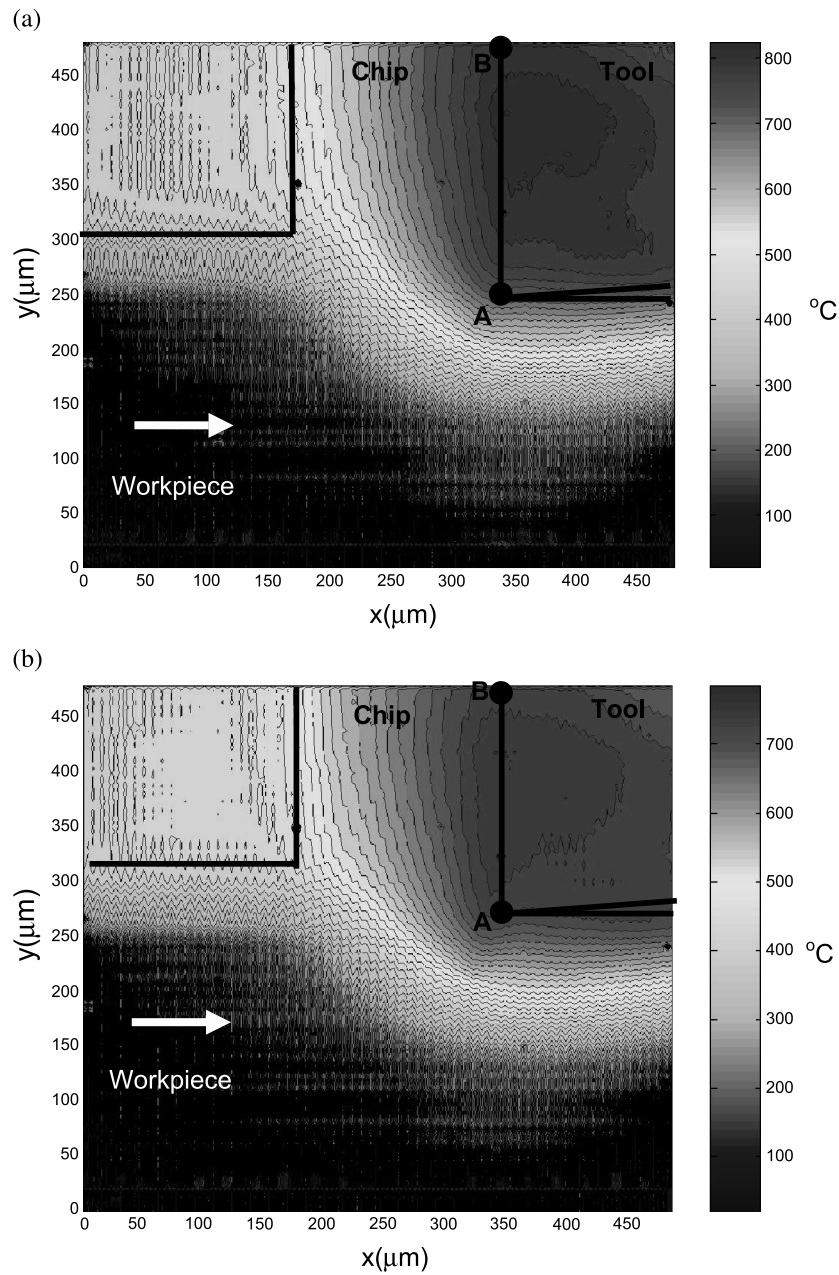
Figure 5. Thermal images of orthogonal cutting of AISI 1045 steel using a surface speed of 3.7 meters per second and chip thicknesses of (a) 48 μm (b) 40 μm. Drawings of the tool and chip are overlaid based upon back lit thermal images and the measured cut chip thicknesses reported in Table 3.

(a)

(b)
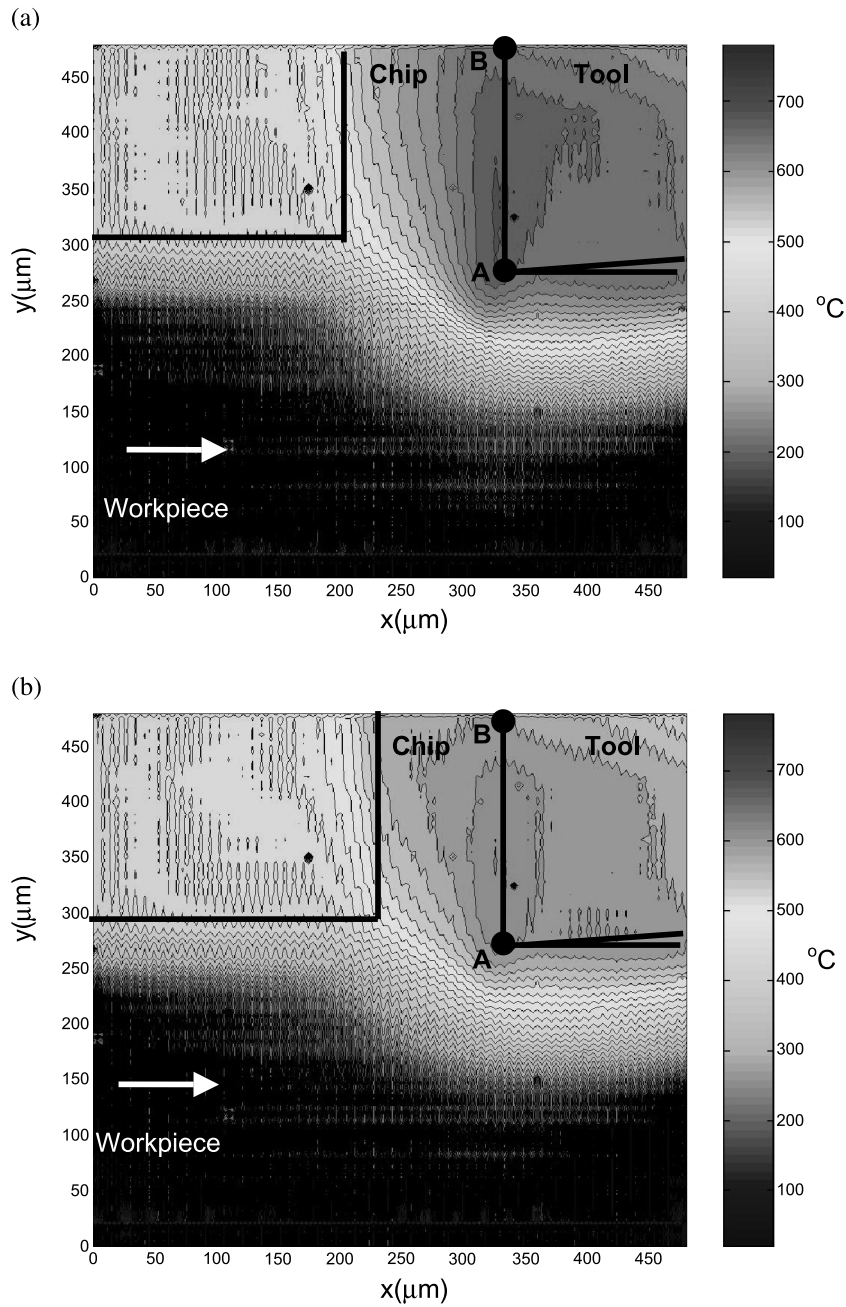
Figure 6.   Thermal images of orthogonal cutting of AISI 1045 steel using a surface speed of 3.7 meters per second and uncut chip thicknesses of (a) 31 μm; (b) 23 μm. Drawings of the tool and chip are overlaid based upon backlit thermal images and the measured cut chip thicknesses reported in Table 3.
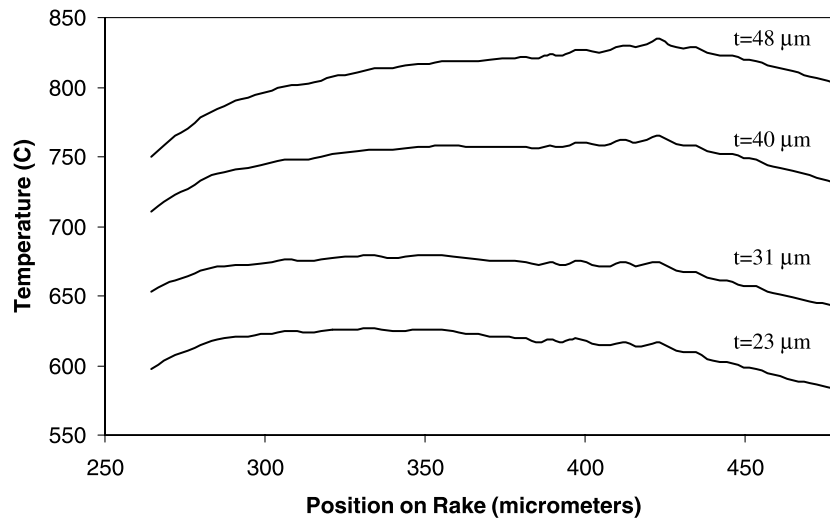
Figure 7. Rake face temperature profiles at different uncut chip thicknesses.

The uncertainty in measurement of the *mean temperature* at each pixel due to the experimental fluctuations was calculated from the 41 images by calculating the standard deviation at each pixel and dividing by the square root of the number of samples. The maximum standard error in the region of interest (i.e. near the tool–chip interface) due to experimental fluctuations is approximately ±14°C, implying that the experimentally obtained steady-state chip formation is quite stable.

Next, to examine the capability of the system to measure systematic variation in the thermal field as a function of a single parameter, the depth of cut was varied as shown in Table 3, experiments 2 through 5. The cutting speed was held constant at 3.7 m/s while the chip thickness was varied. Ten independent measurements were made at each set of conditions. The mean temperatures for each set of ten measurements are shown in Figures 5 and 6. Figure 7 shows individual temperature traces along the rake face of the tool (segment AB) for each of the conditions. The tool tip for each is at the left edge of the graph and the coordinate on the horizontal axis corresponds to the position coordinate on the thermal images. From these traces it can be seen that the peak temperature migrates from a position of approximately 75 micrometers from the cutting edge at an uncut chip thickness of 23 micrometers to a position of greater than 150 micrometers behind the cutting edge for an uncut chip thickness of 48 micrometers. However, despite this migration, the ratio of these values remains fixed at approximately 0.32.

ANALYSIS AND DISCUSSION

Two methods of analysis were employed to further test the validity the experimental measurements. In the first, a control volume approach was used to estimate the total power and the specific cutting energy directly from the thermal

images; these values were compared to the expected values from mechanical power measurements. It is likely that any severe errors in the experimental measurements would be made evident by discrepancies between the calculated and expected results. In the second method, the measured temperatures and trends were compared to an approximate finite-difference method for obtaining temperature distributions attributed to Tlusty (2000). While this method is heavily reliant on empirical data from machining, and can therefore not be classified as a predictive model, *it can be used to further verify the plausibility of the experimental results adding to our confidence in their accuracy.*

Energy Flux Calculations

Knowing the machining parameters and the chip velocity (from conservation of mass), one can estimate the net thermal energy exiting the cutting region using a control volume as shown in Figure 8. Assuming a plane strain deformation, this is accomplished by calculating the energy flux Φ_{ij} flowing through each linear (planar) control surface according to the following equation,

$$\Phi_{ij} = w \int_{P_i}^{P_j} (\rho c T \mathbf{V} - k \nabla \mathbf{T}) \cdot \mathbf{n} ds \tag{8}$$

where: P_i and P_j are the endpoints of the linear (planar) section; s is the spatial coordinate defined along the control surface; $\mathbf{n}$ is the local outward normal to the control volume; V is the local material velocity; T is the local temperature; $\nabla T \cdot n$ is the local thermal gradient; w is the chip width; and k, ρ and c are the thermal conductivity,
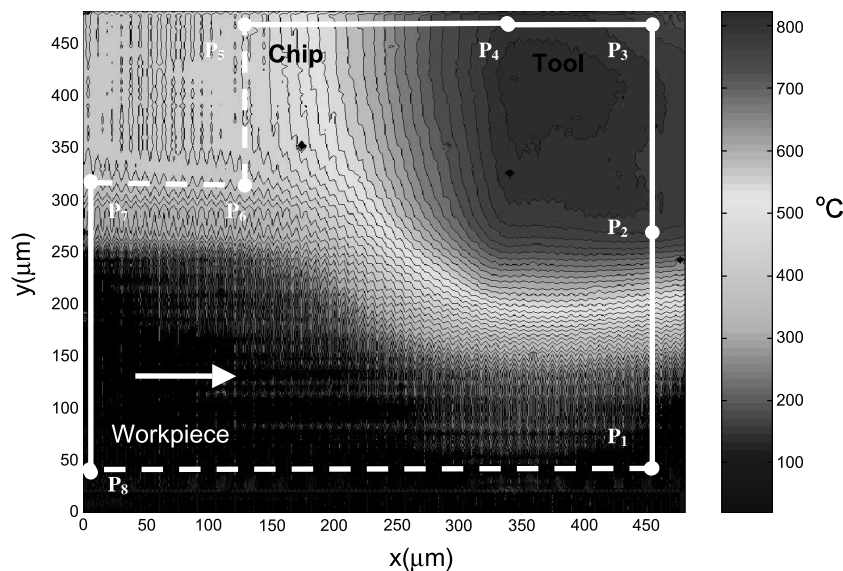
Figure 8. Definition of control volume for specific energy calculations. Dotted lines indicate control surfaces through which negligible energy flows.

density and specific heat capacity of the material respectively. The first term in the integral is the mass transfer term and the second is the conductivity term. This integral is converted to a sum with the step size defined by the spatial resolution of the system. For control surfaces in the tool, the local material velocity and hence the mass transport term is zero. The surfaces represented by the dotted lines in Figure 8 are assumed to have zero energy flux (convection losses to the air are ignored). It is interesting to note that the energy flux into the region due to the influx of workpiece material that was heated during previous repetitive passes of the tool cannot be neglected as it produces a significant negative (inward flowing) energy flux term.

For each of the cases shown in Figures 5 and 6, the net thermal flux exiting the control volume, denoted Φ_{net} was calculated. Assuming that all of the mechanical energy is converted to heat, this net flux is equal to the mechanical power input, P. The results are plotted as a function of uncut chip thickness in Figure 9. The power increases linearly with uncut chip thickness consistent with an increase in cutting force proportional to the chip area. Equating the thermal energy flux exiting the control volume to the total mechanical power results in the following expression,

$$\Phi_{net} = F_c V = K_c t_c w V \tag{9}$$

where F_c is the cutting force and K_c is the specific cutting energy (cutting force coefficient) and t_c and w are the uncut chip thickness and width defined above. From this expression, the specific cutting energy was calculated as a function of chip thickness, and the results are shown in Figure 10. The value remains nearly constant at approximately 2400 N/mm^2 which is consistent with values reported in the literature for low carbon steel (Tlusty, 2000). Finally it was also possible to estimate the percent of the total energy carried away in the chip. This value varied between 78 percent and
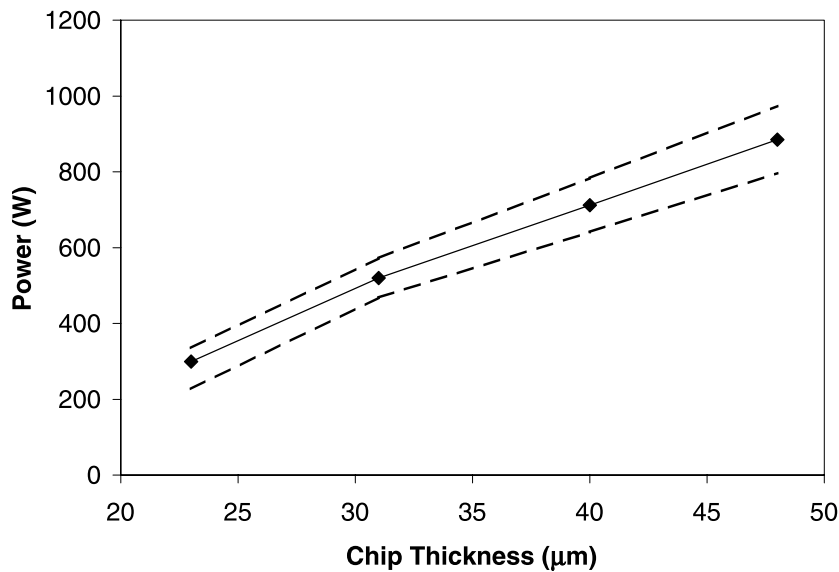
Figure 9. Power versus chip thickness calculated using the control volume approach.
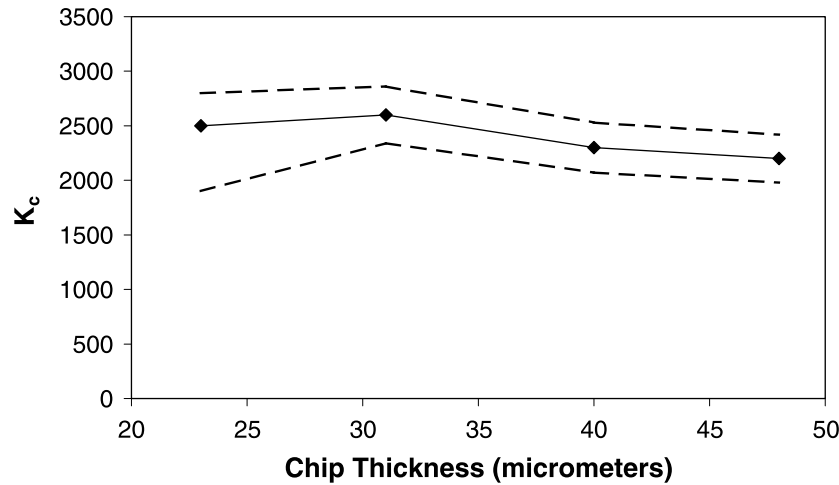
Figure 10. Specific cutting energy versus chip thickness calculated using the control volume approach.

84 percent for the four conditions analyzed here. This is also consistent with expected results (Boothroyd, 1963).

The upper and lower bound curves in Figures 9 and 10 were obtained by numerically varying the position of the control surfaces in accordance with the uncertainties in geometry specified above. Except for the smallest chip thickness where the uncertainties were somewhat larger, this resulted in an uncertainty in flux and specific cutting energy of approximately ±10 percent. The larger uncertainties for the lowest chip thickness appear to result from some uncertainty about the actual chip location in the image. Referring to Figure 6(b), the thermal image indicates that the chip may be curling away from the rake face making the correct location for the control volume surfaces more uncertain than in the other images.

Finite-Difference Simulations

In order to further verify the experimental measurements, finite-difference computations for the temperature field in the chip have also been performed. These calculations follow the single-dimensional transient finite-difference method described by Tlusty (2000) which is a numerical modification of the approach first outlined by Boothroyd.

The finite-difference simulation in Tlusty (2000) defines a two-dimensional grid over the chip area. Two adjacent edges of the grid are bounded by the shear plane and tool–chip interface, respectively, while the remaining edges are assumed insulated (i.e., convection to the surrounding air is taken to be negligible). The shear plane boundary is uniformly heated to the shear plane temperature. The shear plane temperature, T_s, is calculated according to Eq. 10, where K_c is the specific cutting energy of the workpiece material, ρ is the density, c is the specific heat, β is the force angle, ϕ is the shear angle, and T_r is the ambient temperature. A correction factor of 0.8 has been applied to

account for the heat conducting away from the chip into the workpiece (estimated to be 20 percent).

$$T_s = 0.8 \frac{K_s \cos(\beta + \phi)}{\rho c \cos \beta \cos \phi + T_s} \tag{10}$$

The chip temperature field computation proceeds in two stages. In the first stage, heat which escapes from the chip through the tool is neglected. Therefore, all the friction power generated at the tool–chip interface is used as input to heating the chip. In the second, a correction for the power entering the tool is applied. This correction is formulated as single-dimensional steady-state heat flow from the tool–chip contact to the tool-air boundary (at ambient temperature). In both stages, the process power is propagated through the chip by a simplification of the actual steady-state two-dimensional heat transfer problem. The simplified formulation considers mass transfer (of the heat) only in the direction of the chip flow (conduction is neglected) and conduction only in the orthogonal direction (parallel to the shear plane). It is, therefore, a single-dimensional transient heat transfer method that computes the temperatures of a slice of elements parallel to the shear due to power inputs from the shear plane and tool–chip friction interface in discrete time steps. Subsequent time steps, separated by Δt (which is selected for computational stability), follow this slice (in the direction of the chip velocity) from the shear plane to then end of the tool–chip contact length. A comprehensive description of the finite-difference calculations, including relevant equations and example computer code, may be found in Tlusty (2000).

Several physical and empirical parameters are required for the numerical simulation. These values were selected from experimental data and relevant texts or handbooks. Experimental parameters (determined from orthogonal cutting tests in the same workpiece material) included the specific cutting energy, shear angle, and friction angle. Values for the workpiece thermal conductivity, k_{wp}, specific heat and specific mass and tool thermal conductivity, k_t, were obtained from various references. The cutting conditions provided the uncut chip thickness, t, chip width, w, spindle speed, Ω, and cutting speed, V. Relevant values for the four selected cutting tests are listed in Tables 3 and 4 where the shear angles are calculated using the measured cut chip thickness values.

Figure 11 shows the temperatures along the rake face of the cutting tool for the four different chip thicknesses measured in the experiments. The predicted temperature ranges are comparable to those in the measured data (Figure 12), however the shapes are somewhat different. This may imply some systematic inaccuracy in this rather simplified simulation. This is very likely since the simulation relies on guesses about

Table 4. Simulation parameters.

K_c (N/mm^2)	β (deg)	ϕ (deg)	k_{wp} (N/s-C)	c (J/kg-C)	ρ (kg/m^3)	K_t (N/s-C)
2570	30	13	43	474	7800	55
2570	30	13.9	43	474	7800	55
2570	30	15.2	43	474	7800	55
2570	30	16.7	43	474	7800	55
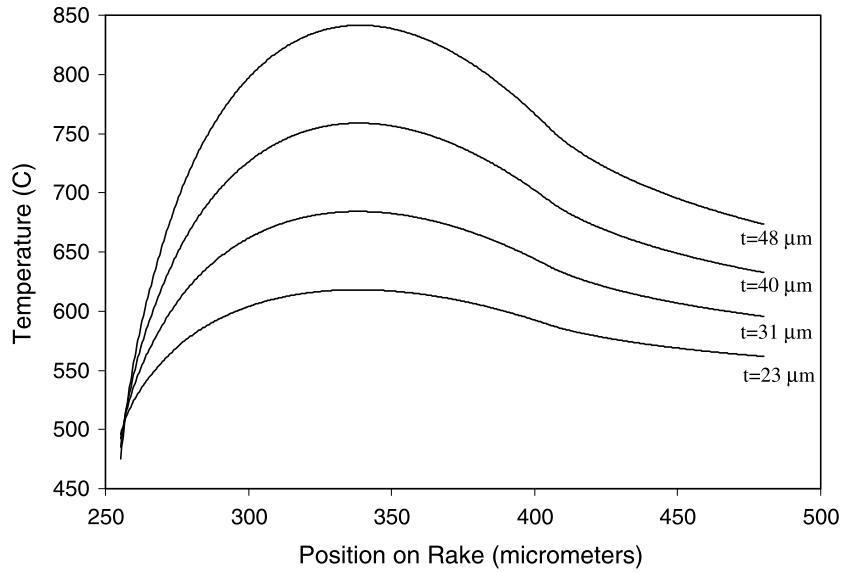
Figure 11. Predicted temperature profiles on the rake face of the tool.

the length of contact between the tool and chip and the generation of heat at the tool–chip interface. However, Figure 12 shows that despite differences in the shape of the curves, the maximum rake temperature obtained from the simulations is the same as the measured maximum temperatures to within the measurement uncertainties. These
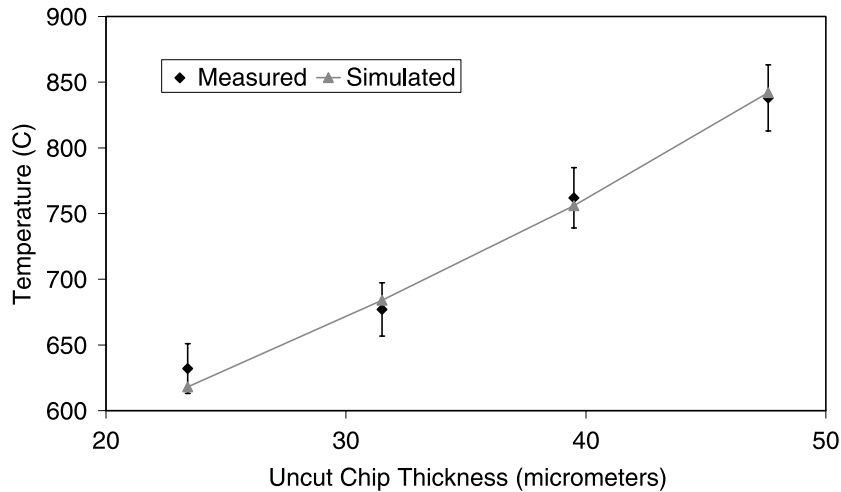
Figure 12. Predicted and experimental maximum temperature as a function of uncut chip thickness. Error bars on experimental data reflect a 15 percent uncertainty in emissivity and a 5 degree C uncertainty in the estimation of the mean temperature due to experimental fluctuations.

simulations further establish the plausibility of the experimental measurements. More detailed finite-element simulations will be required to obtain a more realistic physical model of the system and hopefully provide a better estimate of the shape of the measured interface temperature distribution.

CONCLUSIONS

In this paper, we have demonstrated calibrated microscopic thermal measurements of the tool chip interface during the orthogonal cutting of AISI 1045 steel using an IR microscopy system. The measurement system has approximately a 5-micrometers spatial resolution. The combined standard uncertainty is estimated to be less than 52 degrees C for all of the measurements. Further confidence in the results is afforded by two methods of analysis: 1) calculations of the total thermal energy exiting the cutting region; and 2) finite-difference calculations based upon the method of Tlusty (2000). Using method 1, and equating the thermal energy with the mechanical energy, we were able to estimate the specific cutting energy of the material directly from the thermal images. The values obtained are in agreement with published values for AISI 1045 steel. Although there are some discrepancies in the shape of the predicted and rake face temperature profiles, the finite-difference method also produces results that are consistent with the measurements. The observed differences are to be expected given the large number of assumptions that are needed to develop the model. The next steps in this experimental research effort are to measure a wider range of machining parameters and materials and to modify the microscope to obtain high-bandwidth measurements capable of capturing dynamic phenomena such as shear localization and built-up edge formation.

APPENDIX A: ANALYSIS OF UNCERTAINTY IN EMISSIVITY

The effect of the emissivity variation on the variation in the observed temperature can be calculated using the expressions described in the paper. To do this, we can add a new small parameter ρ to the formulation to represent the expected percent variation in emissivity resulting from the surface deformation and the use of the f/1 geometry in the measurement system. We rewrite Eq. 4 in the following way.

$$R_m = (1 + \rho)\varepsilon(T)R_b(T) \tag{5}$$

The effect of ρ on the uncertainty in temperature will be a function of temperature and it is this relationship we wish to determine. Rearranging and using a Taylor series expansion, we see that the effect of ρ is to lead to an uncertainty in the measured signal R_m.

$$\frac{R_m}{(1 + \rho)} = (1 - \rho + H.O.T.)R_m = R_m - \Delta R_m + H.O.T. \tag{5}$$

where H.O.T. stands for higher order terms which are assumed negligible for small ρ. Thus, our uncertainty analysis for the emissivity reduces mathematically to the
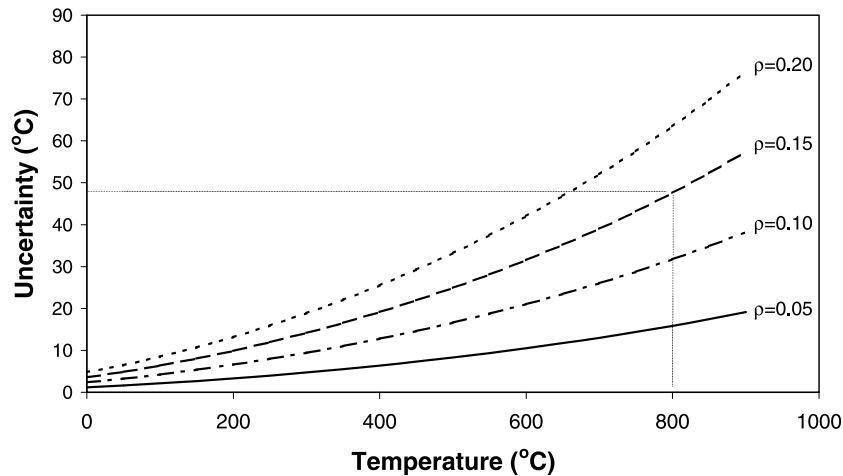
Figure 13. Uncertainty in temperature as a function of temperature for values of the uncertainty in emissivity ranging from 5 to 20 percent.

same problem as an uncertainty in the measured signal. To find the effect of an uncertainty in the measured signal ΔR_m on the uncertainty in the temperature ΔT, we add the small variation in temperature in Eq. 4 and perform a Taylor series expansion on the individual functions. The resulting equation relating ΔT to ΔR_m is developed as follows.

$$\Delta R_m = \left(\frac{\partial \varepsilon}{\partial T} + \frac{\partial R_b}{\partial T} \right) \Delta T \tag{6}$$

Dividing through by R_m and using $R_m = \varepsilon(T) R_b(T)$, we obtain a final approximate relationship for ΔT as a function of the variation in emissivity ε.

$$\Delta T = \frac{\Delta R_m}{\left(\frac{\partial \varepsilon}{\partial T} + \frac{\partial R_b}{\partial T} \right)} \tag{7}$$

Figure 13 shows the relationship between the uncertainty in signal and the uncertainties in temperature plotted for percent uncertainty in emissivity from 5 percent to 20 percent as a function of temperature. A ±15 percent uncertainty in emissivity leads to and uncertainty of approximately ±50 degrees C in temperature at a temperature of 800 degrees C as reflected in Table 1.

ACKNOWLEDGMENTS

Ming Liao for Michigan State University, and Summer Undergraduate Research Fellows, Wendy Shefelbine from Washington University and Forrest Lysinger from Bucknell University and April Cooke from UNC Charlotte.

REFERENCES

Altintas, Y. (2000). *Metal Cutting Mechanics, Machine Tool Vibrations and CNC Design*. Cambridge University Press.

Amarego, E. J. A., Brown, R. H. (1969). *The Machining of Metals*. Englewood Cliffs, NJ: Prentice Hall.

Boothroyd, G. (1961). Photographic technique for the determination of metal cutting temperatures 12:238–242.

Boothroyd, G. (1963). Temperatures in orthogonal metal cutting. *Proc. Inst. Mech. Eng.* 177(29):789–810.

Boston, O. W., Gilbert, W. W. (1935). Cutting temperatures developed by single-point turning tools. *Trans. ASME* 23:703–726.

Ceretti, E., Fallbohmer, P., Wu, W. T., Altan, T. (1996). *Int. J. Mater. Proc. Technol.* 59:169.

Childs, T. (1997). Material property requirements for modeling metal machining. *J. Phys. IV France* 7. Colloque C3, Suppl. Aust. J. Phys. III.

Furness, R. (1998). Modeling of machining operations: an industry perspective. In: Jawahir, I. S., Balaji, A. K., Stevenson, R., eds. Proceedings of the CIRP International Workshop on Modeling of Machining Operations. Lexington: University of Kentucky Publishing, KY, USA.

Hartley, K. A., Duffy, J., Hawley, R. H. (1987). Measurement of the temperature profile in shear band formation in steels deforming at high strain rates. *J. Mech. Phys. Solids* 35(3):283–301.

Herbert, E. G. (1926). The measurement of cutting temperatures. *Proc. Inst. Mech. Eng.* pp. 289–329.

Ivester, R. I., Kennedy, M., Davies, M. A., Stevenson, R., Athavale, S., Furness, R., Theile, J. (2000). Assessment of Machining Models. In: Proceedings of the Third CIRP International Seminar on Modeling Machining Operations, Sydney, Australia.

Jawahir, I. S. (1999). In: Panel Presentation at the International Mechanical Engineering Congress and Exposition. Nashville, TN, November.

Marusich, T. D., Ortiz, M. (1995). *Int. J. Numer. Methods Eng.* 38:3675.

Merchant, M. E. (1998). An interpretive look at 20th century research in modeling of machining. In: Jawahir, I. S., Balaji, A. K., Stevenson, R., eds. Proceedings of the CIRP International Workshop on Modeling of Machining Operations. Lexington: University of Kentucky Publishing, KY, USA.

Meyers, M. *Dynamic Behavior of Materials*, complete reference.

Movahhedy, M.-R., Altintas, Y., Galada, M. S. (2000). Numerical analysis of cutting with chamfered and worn edges. To appear in the Proceedings of the IMECE 2000.

Oxley, P. L. B. (1989). *The Mechanics of Machining: an Analytical Approach to Assessing Machinability*. Prentice Hall.

Palik, E. D., ed. (1991). *Handbook of Optical Constants of Solids II*. San Diego: Academic Press, Inc.

Saeki, I., Konno, H., Furuichi, R. (1996). The initial oxidation of type 430 stainless steel in $O_2-H_2O-N_2$ atmospheres at 1273 K. *Corros. Sci.* 38(1):19–31.

Sakuma, F., Kobayashi, M. (1996). Interpolation equations of scales of radiation thermometers. In: Proceedings of the Tempmeko '96.

Stephenson, D. A. (1993). Tool–work thermocouple temperature measurements—theory and implementation issues. *ASME J. Eng. Ind.* 115:432–437.

Strenkowski, J. S., Carroll, J. T. III. (1986). An orthogonal metal cutting model based on an Eulerian finite element method, manufacturing processes, machines and systems. In: Proceedings of the 13th NSF Conference on Production Research and Technology.

Tlusty, G (2000). *Manufacturing Processes and Equipment*. Prentice Hall.

Trent, E. M. (1991). *Metal Cutting*. Butterworth-Heinemann Ltd.

Trigger, K. J. (1948). Progress report no. 1 on tool–chip interface temperatures. *Trans. ASME* February, pp. 91–98.

van Luttervelt, C. A., Childs, T. H. C., Jawahir, I. S., Klocke, F., Venuvinod, P. K. (1998). ''Present situation and future trends in modelling of machining operations,'' progress report of the CIRP working group 'Modelling of Machining Operations'. *CIRP Ann.* 47(2):587–626.